Experimental study of the effect of wind above irregular waves on the wave-induced load statistics

Julie Carøe Kristoffersen, Henrik Bredmose, Christos Thomas Georgakis, Hubert Branger, Christopher Luneau

Experimental study of the effect of wind above irregular waves on the wave-induced load statistics

Julie Caroee Kristoffersen[a,*,1], *Henrik Bredmose*[b], *Christos Thomas Georgakis*[a], *Hubert Branger*[c], *Christopher Luneau*[d]

[a]*Department of Engineering, Aarhus University, Inge Lehmannsgade 10, DK-8000 Aarhus, Denmark*
[b]*DTU Wind Energy, Nils Koppels alle bulding 403, DK-2800 kgs. Lyngby, Denmark*
[c]*IRPHE, CNRS, AMU, ECM, Campus Luminy, Bat IOA, FR-13009 Marseille, France*
[d]*Institut Pythéas, CNRS, AMU, IRD, Campus Luminy, Bat Pythéas, FR-13009 Marseille, France*

Abstract

The design load from waves on offshore structures are often estimated by aid of experimental studies in wave flumes and basins. When going from open sea to laboratorial conditions a number of factors are either added or omitted such as wind above waves. The paddle-generated waves are based on a spectrum taking the indirect effect of wind into account, whereas the direct effect of wind is left out. Previous studies have focused on the direct effect of wind on waves themselves, but no investigations on the load has been made. The question is whether or not airflow separation, vortexes etc. in the wind field alter physical properties such as steepness of waves, the number of breaking waves and hereby the depth-integrated force. To investigate the matter, an experimental study of depth-integrated force on a circular cylinder from irregular waves both with and without wind above was conducted. An objective, when conducting the tests, was to achieve the same significant wave height whether wind was present or not. Exceedance probability curves for wave crest height, depth-integrated force and pressure were obtained. Moreover, a more descriptive assessment of the phenomena was done by studying the average force shape of the hundred largest force events. In addition, a phase-based harmonic separation method to explore the wind's effect on the harmonic force content of higher order was applied. The front steepness of the waves was clearly increased with the introduction of wind and further increased, when increasing the wind velocity. The introduction of wind consistently increased the number of breaking waves detected with a breaking criterion. The wave-induced load in the tail of the exceedance probability curve was only increased for some of the sea states, when wind was added. This was very dependent on the crest height of the waves that was forced to break. The maximum wave-induced pressure in the tail of the exceedance probability curve was on the contrary increased for all sea states, when wind was present, and it kept increasing with increasing wind velocity. For one of the sea states with increased force extremes, the averaged force shape for the hundred largest events of a case with wind revealed a force shape with a spiky peak consistent with that generated from breaking waves. This was not present for the case without wind. The separated harmonic content of the force up to fourth order also showed a tendency towards more energy at harmonic components of higher order for the case with wind.

Keywords

Offshore structure; Wave-induced load; Direct wind effect on waves; Irregular waves;

[*] jck@cae.au.dk (J. C. Kristoffersen)

1. Introduction

For the design of offshore structures, force statistics of waves are an inevitable requirement. The statistics are obtained by using site-specific hind cast data along with numerical or experimental realizations of irregular waves for representative sea states. A site-specific spectrum such as Jonswap-spectrum or Bretschneider-spectrum is applied in order to generate irregular waves. The indirect effect of wind is hereby taken into account through its influence on the spectral parameters. Utilizing the wave-induced loads from the irregular waves on a test object, gives an exceedance probability distribution and finally an estimate of the design load. Different uncertainties are coupled to the experimental process such as scaling issues and a number of factors either omitted or added in laboratory conditions. One of the omitted factors is the direct effect of wind above waves, which is addressed in this paper. The direct effect can for instance be present, when the airflow in the wind above the waves is separated. The flow field thereby results in added energy transfer from the wind to the waves [1],[2]. Recently, the airflow separation in a wind field over focused wave trains have been studied both experimentally and numerically with emphasis on the change of the wave amplitude. The experimental findings of [3] showed that with the introduction of wind, the waves remain focused for a longer duration and obtain a slight increase in amplitude. Tests with Digital Particle Image Velocimetry [4] reveal another consequence of wind above waves, namely that airflow separation over very steep waves results in vortices on the leeward side of the wave. This adds to the energy transfer from the wind field to the waves. The matter is confirmed in numerical simulations where both the wind's effect on waves and vice versa were modelled [5]. The waves are steepened by the wind pressure variations from wave trough to trough appearing due to vortexes. The airflow separation was also investigated in an experimental study [6], in which registration of airflow separation was enabled by means of a well-designed equipment setup including hot and cold X-wires. The observations show that the separation occurs once the local wave slope exceeds 0.35 m/m and that it is often followed by wave breaking. This sort of energy transfer from the wind field will even occur for waves in a fully arisen sea, and it will naturally be balanced by continuous breaking dissipation from breaking waves. It can potentially give a distribution of the wave steepness different from that generated in laboratory conditions without wind, i.e. the wave steepness can be considerably different for realizations with and without wind having the same significant wave height. In the open sea where the direct effect of wind is naturally present, the waves would be steeper, the number of breaking waves higher, and the load statistics thereby increased for a certain sea state compared to that obtained in laboratorial conditions without wind, i.e. the load statistics obtained in the laboratory would be underestimated. Wind stress above water waves may also change the surface currents and increase the local vorticity under the water surface [7], which may alter the loads on marine structures. Moreover, another concern is raised since numerical simulations [8] show that wind above waves speeds up the overturning crest. If this is realistic for physical water waves, the load from breaking waves could be increased, when wind is present, and the tail of the exceedance probability curve for loads would change. This change of wave-induced load caused by the influence of wind above focused waves was studied numerically in [9]. For an initial non-breaking wave, the wind ultimately forces the wave into breaking and thereby increases the load significantly. For an initial breaking wave, the wind drives the wave to break earlier and the load is actually slightly decreased. However, a high velocity of the wind above steep focused waves can result in increased wave-induced pressure. Since the modelling of breaking waves in the applied numerical code, OceanWave3D [10] is uncertain, an experimental study is necessary. An experimental study is required to clarify both the wind's effect on individual large and breaking wave and on the load statistics of irregular waves.

In the present paper, the exceedance probability distribution for wave crest height, wave-induced load and pressure was obtained in experiments consisting of irregular waves with and without wind to evaluate the influence of wind above waves. The frame of reference was improved by ensuring that difference between the significant wave height in tests with and without wind was within +/-5%. Moreover, characteristics of the waves such as crest height

and steepness were evaluated in relation to a breaking criterion to clarify the differences in the force statistics. To explore the consequences of direct effect of wind, we present an in-depth investigation of the average shape of the largest force events and of the higher order force components obtained with a phase-based separation method. The methodology of these investigations is presented in the next section. Next, the paper continues with a description of experimental setup, results and discussion to elaborate on the hypothesis that the direct effect of wind alters the waves' steepness and more importantly the exceedance probability curve of the wave-induced load and pressure.

2. Methodology

2.1 New Force method

The most probable wave shape around a crest peak can be described by New Wave theory [11], which is based on the auto correlation function of the wave spectrum. The largest force peak, however, does not have to be generated from the largest wave, but depends also on the steepness. The most probable shape of the force around a peak is therefore described by the New Force concept [12]. The linear force spectrum is described as

$$S_F(\omega_j) = |\Gamma(\omega_j)|^2 \, S_\eta(\omega_j), \tag{1}$$

where $\Gamma(\omega_j)$ is the force transfer function, ω_j the wave frequency of the jth component and $S_\eta(\omega_j)$ the wave spectrum. The most probable shape around a force peak can then be derived from the linear force spectrum as

$$F^{(1)}_{NewForce} = \frac{\alpha_F}{\sigma_F^2} \sum_j Re\left\{|\Gamma(\omega_j)|^2 \, S_\eta(\omega_j)\, \Delta\omega \cdot exp\left(i\,(\omega_j(t-t_0) - k_j(x-x_0))\right)\right\}, \tag{2}$$

where α_F is the value of the force peak, σ_F is the standard deviation of the linear force spectrum, k_j is the wave number of the jth component given by the dispersion relation $\omega_j^2 = g\, k_j \tanh(k_j\, h)$, where g is the gravitational constant, h is the water depth. The focal point is x_0 and t_0 the focal time. Superscript indicates the order. The corresponding surface elevation is then given as

$$\eta^{(1)}_{NewForce} = \frac{\alpha_F}{\sigma_F^2} \sum_j Re\left\{\Gamma^*(\omega_j)\, S_\eta(\omega_j)\, \Delta\omega \cdot exp\left(i\,(\omega_j(t-t_0) - k_j(x-x_0))\right)\right\}, \tag{3}$$

where Γ^* is the complex conjugate of Γ. The second order force is estimated from Morison's equation [13] and the force model of [14], where the applied second order surface elevation and wave kinematics are calculated by use of second order wave theory [15].

$$F^{(2)} = \rho\,\pi\,R^2 C_M \int_{-h}^{0} (u_t^{(2)} + u^{(1)} u_x^{(1)} + w^{(1)} u_z^{(1)})\, dz + \rho\,\pi\,R^2\,(C_M - 1) \int_{-h}^{0} (u^{(1)}\, w_z^{(1)})\, dz +$$

$$\rho\, R\, C_D \int_{-h}^{0} (u^{(1)}\,|u^{(1)}|)\, dz + \rho\,\pi\,R^2 C_M\, \eta_{NF}^{(1)}\, u_t^{(1)} \tag{4}$$

Here R is the radius of the cylinder, ρ is the density of water, h is the water depth, C_M and C_D the inertia and drag coefficient. The velocity in x- and z-direction are denoted by u and w, respectively. Subcase indicates derivation and superscript the order. This New Force model will be compared to the averaged force time series around the peak of the ten largest force events in the tests both with and without wind. This part is elaborated in the results section.

2.2 Phase-based harmonic separation

To assess the content of the higher order force components, the force can be separated in first, second, third, fourth order super harmonics and second order subharmonic by implementation of a four-phase based harmonic separation [16], which is expanded from the two-phase based separation of [17]. Four time series of the force were obtained in the irregular wave tests, where the phase of the wave paddle signal was shifted with 0, 90, 180 and 270 degrees, respectively. These can then be applied in order to separate the different harmonic components of the force. If the composition of the force is assumed as a perturbation expansion, it can be described as

$$F = A f_{11} \cos\varphi + A^2 \left(f_{20} + f_{22}\cos 2\varphi\right) + A^3 \left(f_{31}\cos\varphi + f_{33}\cos 3\varphi\right) + A^4 \left(f_{42}\cos 2\varphi + f_{44}\cos 4\varphi\right), \quad (5)$$

where A is the wave amplitude, f_{nm} is the wave-to-force transfer function and $\varphi = \omega t + \varphi_0$ is the phase of the wave, with φ_0 the initial wave phase. The different force components from first to fourth order are extracted from

$$(F_0 - F_{90}^H - F_{180} + F_{270}^H) / 4 = A f_{11} \cos\varphi + A^3 f_{31} \cos\varphi + O(A^5) \quad (6)$$

$$(F_0 - F_{90} + F_{180} - F_{270}) / 4 = A^2 f_{22} \cos 2\varphi + A^4 f_{42} \cos 2\varphi + O(A^6) \quad (7)$$

$$(F_0 + F_{90}^H - F_{180} - F_{270}^H) / 4 = A^3 f_{33} \cos 3\varphi + O(A^5) \quad (8)$$

$$(F_0 + F_{90} + F_{180} + F_{270}) / 4 = A^2 f_{20} + A^4 f_{44} \cos 4\varphi + O(A^6), \quad (9)$$

Where F_0, F_{90}, F_{180} and F_{270} are the load induced on the model from waves generated with the wave paddle signal shifted with 0, 90, 180 and 270 degrees, respectively. Superscript H means application of the Hilbert operator. The first, second, third and fourth order components are determined respectively with eq. (6), (7), (8) and (9). It should be noticed that eq. (9) also contains the second order subharmonic force, which can easily be separated from the fourth order due to the large separation in the frequency domain. The higher order force components can now be compared in the test cases with and without wind to explore if a wind field adds to the higher order force components. This is elaborated in the results section as well.

3. Experimental setup

The tests were conducted in the Large Air-Sea Interface Facility of the IRPHE/Pytheas laboratory at Luminy University, Marseille, France. The facility consists of a 40.0 x 2.6 x 0.9 m wave tank with a 40.0 x 3.2 x1.5 m closed-loop airflow channel on top. A complete description of the facility with schematic views can be found in [18]. The tunnel roof is carefully profiled to create an airflow boundary layer of zero pressure gradient along the test section. At the downwind end of the tank a permeable absorbing beach is installed to minimize wave reflection. The wave tank is equipped with a mechanical wave paddle. The computer-controlled wave-maker can generate regular or random waves and it is entirely submerged under the upstream beach to avoid any perturbation of the air flow which could be induced by its displacement. The airflow channel has a turbulent grid, convergent and divergent sections designed to obtain a homogeneous flow at the entrance near the wave paddles, and hereby achieving a natural development of the air boundary layer at the water surface. This gives a logarithmic wind profile throughout the tank. The tests were Froude scaled 1:100 to obtain dynamic similitude. The model used for investigation of wave-induced load, was a fixed-fixed circular pipe made of aluminum. The model setup, which is shown in figure 2, contains a load cell right above the bottom fixing and a load cell below the top fixation. It had a height of 1.3 m and a diameter of 0.1 m, corresponding to 10 m full scale. The first natural frequency was

determined to 65.6 Hz by means of operational modal tests, where the model was excited with white noise loading applied with a soft brush. The water depth used in the tests was 0.9 m. The irregular waves in the tests were generated from a Jonswap spectrum with peak frequencies varying from 0.80 and 1.05 Hz. The model therefore had a stiffness allowing for adequate separation between the dynamic force components and the wave-induced load. The water elevation was measured with four different DANTEC 55E capacitance wave gauges. Wind speed reference at the entrance of the air channel was measured with a Windsonic GILL anemometer. Wind turbulence near the model was measured with a DANTEC CTA hotwire anemometer. The applied equipment and their sampling frequency are listed in table 1. The location of wave gauges, hotwire and the model can be seen in figure 1. The position of wave gauges 1 and 2 was chosen to obtain measurements suitable as reference signal for the purpose of numerical simulations, whereas wave gauges 3 and 4 are used for statistical assessment of wave height, crest height, temporal and spatial slope. The position of load cells, pressure transducers and accelerometers is shown in figure 2 and the vertical distance from the bottom of the tank up to the sensors is listed in table 2. Horizontally, the pressure transducers and accelerometers were placed as seen in figure 3. A photo of the model in working position with the equipment is found in figure 4. All sensors acquired data through a National Instruments module connected to a DAQ chassis, whereby synchronization of data was ensured. The setup with model and load cells was calibrated in static tests by means of a dynamometer and weights.

Table 1: Overview of applied equipment and sampling frequency.

Sensor Type	Number of sensors	Sampling frequency [Hz]
DANTEC 55E capacitance wave gauges	4	1024
DANTEC single sensor CTA hotwire	1	1024
ATI Force-Torque load cells	2	6400
Kulite XTL-190M pressure transducers	8	6400
Brüel and Kjær 4508-B axial accelerometers	8	6400
WindSonic Gill Anemometer	1	1
National Instruments Compact DAQ	1	

Table 2: Vertical position of sensors

Pressure transducers	z [m]	Accelerometers	z [m]
1	0.79	1	0.79
2	0.84	2	0.87
3	0.89	3	0.95
4	0.94	4	1.02
5	0.99	5	1.09
6	1.04	6	1.16
7	1.09	7	1.00
8	1.14	8	1.09

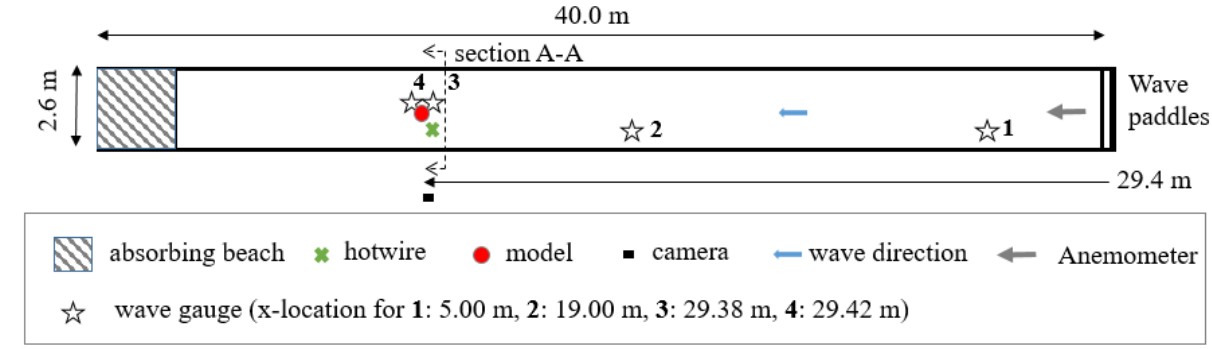

Figure 1: Position of wave gauges, hotwire and model along the wave tank. Location of wave paddles and absorbing beach.

166

167

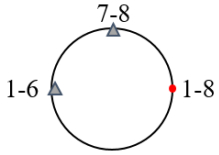

Figure 2: Horizontal position of sensors on model

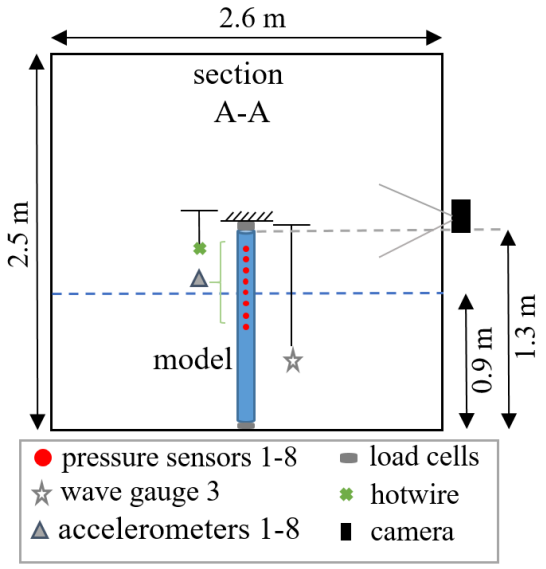

Figure 3: Vertical position of wave gauge, hotwire, accelerometers and pressure sensors on the model.

Figure 4: Photo of the model in working position.

Sea States

In total four different sea states were considered to explore the wind effect and its dependency on the steepness of the sea states. Irregular waves were generated from a Jonswap spectrum with gamma value of 3.3 and a frequency interval of 0.3-1.9 Hz. The parameters of the four sea states are listed in table 3. The sea states were run for 18 minutes corresponding to a 3-hour full-scale sea state. Every 18 minutes sea state test were repeated ten times but with different random phases of the wave maker signal to ensure statistical independency. Moreover, four 18-minutes time series of irregular waves were ran with 0, 90, 180 and 270 degrees phase shift to enable separation of harmonic force components. The repeated tests of sea state A, B, C and D were conducted at two different wind velocities, namely of 0.0 m/s and 5.5 m/s, which was measured 1.0 m above the still water level at the entrance of the flume with the sonic anemometer. Sea state B and D were also conducted at a wind velocity of 7.0 m/s. The wave maker signal of the tests with wind velocity of 5.5 m/s and 7.0 m/s was multiplied with a reduction factor to achieve same significant wave height, H_s as in the tests without wind. This means that the increase in H_s at the location of the model caused by the added energy from wind to waves along the tank was compensated by generating a reduced signal at the beginning of the tank. The reduction factor, p_{red} for different sea states and corresponding wind velocities is listed in table 3. The reduction factor p_{red} was calibrated by experimental iteration for one of the ten repetition tests. For the sea states of lowest H_s the wind-generated waves constituted a larger percentage of the total wave height and the paddle-generated waves were more reduced thus giving a lower reduction factor, p_{red} for sea state A and C.

Table 3: Sea state parameters: Peak frequency, f_p and significant wave height, H_s for the sea states, and reduction factor, p_{red} on the wave paddle signal for wind velocity 5.5 and 7.0 m/s

	f_p [Hz]		H_s [m]		p_{red} for velocity	
Sea state	Model scale	Full scale	Model scale	Full scale	5.5 m/s	7.0 m/s
A	1.05	0.105	0.080	8.0	0.78	-
B	0.95	0.095	0.090	9.0	0.92	0.80
C	0.95	0.095	0.080	8.0	0.85	-
D	0.80	0.080	0.095	9.5	0.92	0.88

Scaling of wind

The scaling of the force is Froude scale to achieve dynamic similitude. The wind forcing from the aerodynamic pressure, is according to Jeffrey's sheltering mechanism [19], $p = \rho_a S(u - c_\varphi)^2 \eta_x$, where ρ_a is density of the air, S a sheltering coefficient, u the velocity of the wind, c_φ the wave phase velocity and η_x local wave slope. The velocity of the wind is therefore scaled with the square root of the length scale. The largest mean velocity measured at 48.0 m above still water level near the Maersk Oilrig, Endeavour is 51.4 m/s and the largest wind gust was 59.2 m/s [29]. Assuming a logarithmic wind profile, the horizontal velocity as function of vertical coordinate is described as $u(z) = \frac{u^*}{\kappa} ln\left(\frac{z}{z_o}\right)$, where u^* is the friction velocity, κ is Von Karmen constant and z_o is the roughness length. Applying the parameters $\kappa = 0.4$, $z_o = 1.2 \cdot 10^{-4} m$ and u^*=*1.6* and u^*=*2.1* m/s, which are in accordance with the friction velocities and roughness lengths recorded in very high wind conditions [20] [20], results in the full-scale wind velocity profiles seen in figure 5. The velocity 10 m above sea water level, u_{10} equals 45.7 m/s and 58.0 m/s, which scales to 4.57 m/s and 5.80 m/s at model scale. The lowest wind velocity of which tests of irregular waves are conducted, is chosen in between these observation events, namely of 5.5 m/s. We assume that, the wind velocity follows the same statistical trend as the relation between the maximum wave height in 10,000 year and significant wave height. That relation is given as $H_{max,10,000y} = H_s \cdot \sqrt{\log(10000)/2}$, where it is assumed that the wave heights follow a Rayleigh distribution. The maximum mean wind velocity of 45.7 m/s is observed over a period of 50 years. The largest wind velocity used in the tests should correspond to a 10,000 year wave, and is therefore calculated to $\langle u_{max,10000} \rangle = \langle u_{max,50} \rangle \frac{\sqrt{\log(10000)/2}}{\sqrt{\log(50)/2}} = 4.57 \cdot \frac{2.15}{1.40} = 7.0$ m/s

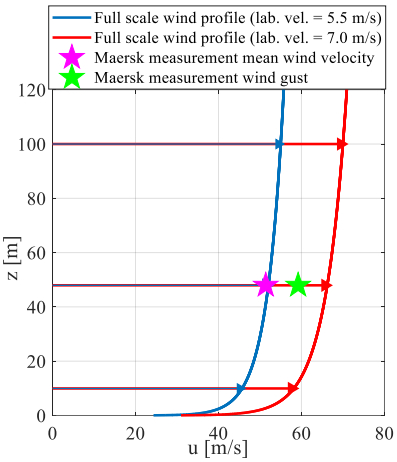

Figure 5: Full-scale logarithmic wind profile, where the velocity 100 m above the mean water level, u_{100} corresponds to model-scale velocity, of 5.5 and 7.0 m/s 1 m above mean water level (Froude scaled). The stars mark extreme measurements on Maersk Oilrig Endeavour.

4. Direct effect of wind on waves and wave loading

This study of the effect of wind above waves and the wave-induced loads was focused on unidirectional irregular waves of four sea states. The overall severity of these sea states was evaluated by plotting the nondimensional steepness against the nondimensional depth in the wave theory diagram [22] in figure 6. The peak period, T_p and wave depth, h was applied with both the significant wave height, H_s marked with red stars and the theoretical maximal wave height for 10,000 waves, $H_{max,10,000}$ marked with magenta dots. The waves of the sea states were ranging from intermediate to deep water waves and were for wave heights equal to the significant wave height adequately described with Stokes third order theory. The highest waves in the sea states were nevertheless highly nonlinear. The actual steepness of the waves in the tests of different sea state parameters are investigated along with Kjeldsens breaking criterion [23], where the waves are determined to be breaking when $\varepsilon > 0.32$ with ε defined as sketched in figure 8.

4.1 Effect of wind on waves in terms of significant wave height, crest height and steepness

The focus in this section is how a wind field above the waves affects the steepness, crest height and other characteristics of the waves. The sea states consist of irregular waves of different severity from the state where more than one percentage of the waves are breaking to that where hardly none are breaking. The development of the irregular waves along the tank is plotted in figure 7 in terms of significant wave height for all wind velocities.

This is done to explore how energy is transferred from the wind to the waves and how energy is dissipated through wave breaking. It should be mentioned that the first mark at a fetch of 0.0 m is an input H_s to the wave maker and not a calculation of H_s based on measurement, since no wave gauge was present at that fetch. For all sea states without wind the significant wave height, H_s is larger at the fetch of 5.0 meters than the input H_s, which could be explained with either a wrong calibration of that wave gauge or by a difference in the input to the wave maker. For sea state A with wind velocity of 0.0 m/s, the significant wave height is reduced throughout the tank from the fetch of 5.0 meters to 29.4 meters due to breaking dissipation. On the contrary, it is maintained throughout the tank, when wind is introduced and the winds energy input balances the breaking dissipation. This means that the significant wave height is 3.8 % larger at the model for tests with wind. For sea state B without wind, the significant wave height is moreover largely reduced from the fetch of 5.0 meters to that of 29.4 meters. For wind velocity of 5.5 m/s the significant wave height exceeds that for wind velocity of 0.0 m/s at a fetch of 5.0 meters. From 5.0 meters and further down tank, it is decreasing, but not as much as in tests without wind, so it ends up being 4.4 % larger at the model. The significant wave height for 7.0 m/s is 5.0 meters down tank the lowest, but the wind energy transfer evens out the breaking dissipation and it end up at the same value as for tests without wind. For sea state C, there is a reduction in the significant wave height for tests with wind velocity of both 0.0 m/s and 5.5 m/s from a fetch of 5.0 meters to one of 29.4 meters. It seems however, as the wind is transferring energy to the waves, since the reduction is smallest for the tests with wind, and therefore the significant wave height builds up being 2.5 % larger at the model. For sea state D, the reduction of the significant wave height from a fetch of 5.0 meters to one of 29.4 meters is decreased as the wind velocity increases. This suggests that the higher wind velocity, the higher increase in total energy until a certain limit is reached. However, the energy dissipation is still dominating. The significant wave height 29.4 meters down tank is the same for wind velocity of 0.0 m/s and 5.5 m/s, whereas is it 2.1 % larger for tests with wind velocity of 7.0 m/s. The objective to have the same significant wave height at the model for all wind velocities was difficult to reach, since the reduction factor was only calibrated for one of the ten repetition tests, but it is still in a range, which provides a reasonable benchmark.

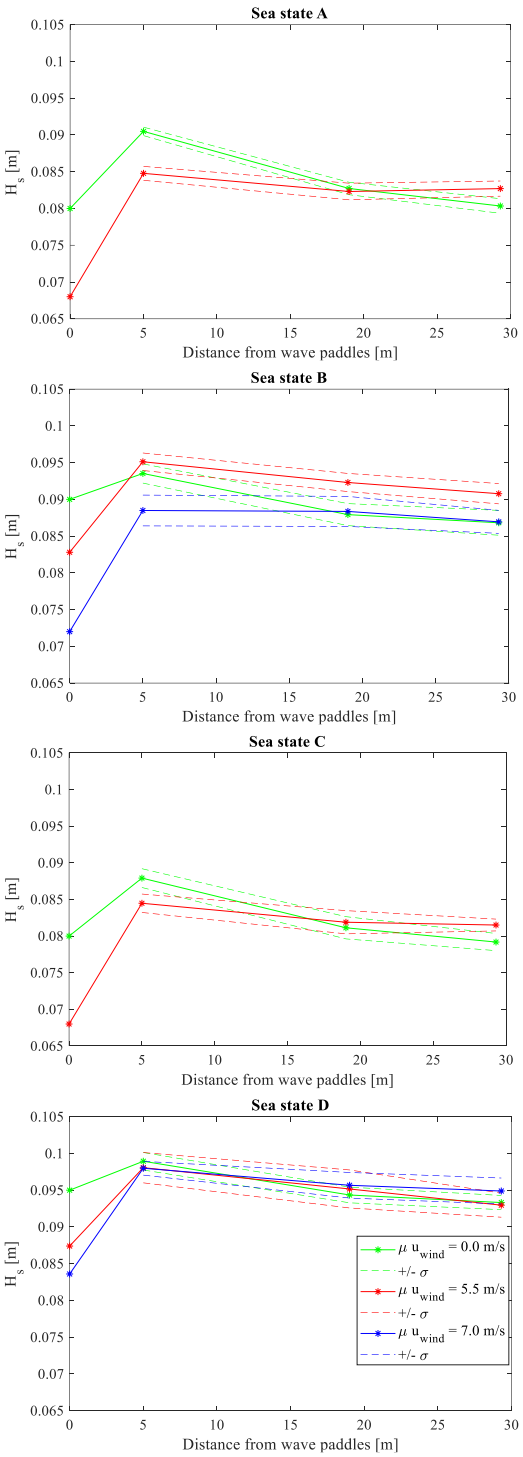

Figure 6: The development of significant wave height, H_s along the wave tank measured with four wave gauges, which position are marked in figure 1. The first point is the input H_s to the wave maker. The last point is the average significant wave height of wave gauge 3 and 4. H_s is plotted for sea state A-D with wind velocity of 0.0, 5.5 and 7.0 m/s.

We now analyze the effect of wind on the individual wave properties of crest height and steepness for each sea state. To achieve statistics for wave crest height, steepness, wave-induced load etc. a zero-down-crossing analysis was performed on the 18-minutes signals of the surface elevation measured with wave gauge 3 right in front of the model. The signal was low-pass filtered up to 1.9 Hz before doing the zero-down-crossing analysis to avoid detecting very short and small waves. These smaller fluctuations in the surface elevation were more pronounced in tests with wind, which is seen in the wave spectrum of wave gauge 3 in figure 8. We see that there is more energy at frequencies higher than 2 Hz, when wind is introducing. This increase in the power spectrum at these frequencies goes well in line with the frequencies of the small ripples generated by the wind. These small ripples will inevitably cause a different profile of the surface elevation of the waves. However since the significant wave height, H_s is decreased in the tests with wind, there still is a fair benchmark for comparison. The crest and wave height between the already determined zero-down-crossings was found for the originally unfiltered wave gauge signal to avoid an underestimation of the wave height. For the breaking criterion of Kjeldsen [23] a definition for the length, crest height and steepness of the wave front was applied, which is shown in figure 7. In addition, the wave period was adjusted to the period of the unfiltered signal to avoid an overestimation of this parameter. The crest height is plotted against the length of the front of the highest 500 waves in terms of crest height in figure 9. The mean front length and the mean crest height of the wave population is marked with a larger, darker dot to observe how they are changing, when wind is introduced. The black line marks the breaking limit of Kjeldsen [23] i.e. the waves to the left of the line are determined to be breaking. For sea state A and C it can be seen that the mean front length is decreased, whereas the mean crest height is hardly changed, when wind is increased from 0.0 to 5.5 m/s, meaning that the waves are steepened. This is confirmed in table 4, where we can see that the crest height is only increased with 1.7 % and 1.9 % respectively for sea state A and C, whereas the length of the wave front is decreased with 5.3 % and 6.5 % for sea state A and C. For sea state B and D the mean is moved both upwards and to the left, when wind is increased from 0.0 m/s to 5.5 m/s. This is confirmed in the table 4, where there is an increase in the average crest height of respectively 8.8 % and 6.1 % and a decrease of respectively 8.4 % and 7.6 % on the average length of the wave front for sea state B and D. This means that the mean crest height and the mean steepness of the top 500 waves of sea state B and D are both increased, when wind is present. When the wind is increased from 5.5 m/s to 7.0 m/s the effect is however, less pronounced. For sea state B, the crest height is even slightly decreased, but the length of the wave front is still decreased.

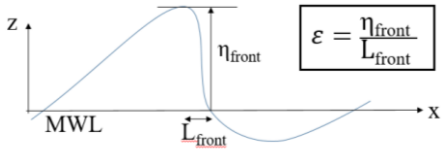

Figure 7: Definition of length and crest height of a wave front applied in [23]

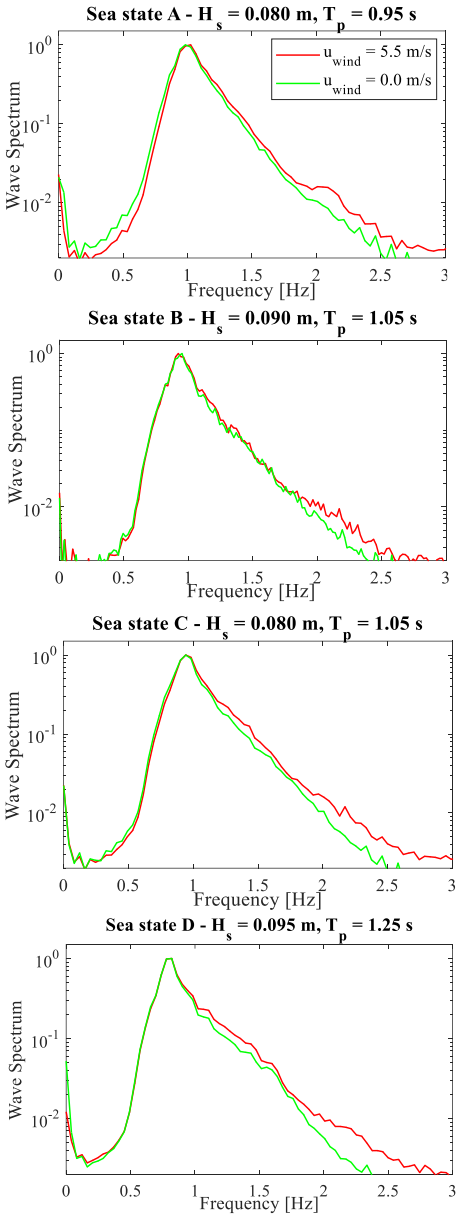

Figure 9: Wave spectrum for all sea states A-D with wind velocity of 0.0 m/s and 5.5 m/s. The green line is for tests with wind velocity of 0.0 m/s and the red line is for tests with wind velocity of 5.5 m/s.

For sea state D, the crest height is increased and the length of the wave front is decreased, meaning that the waves are steepened, when going from a wind velocity of 5.5 m/s to 7.0 m/s. For all sea states, it can be observed in figure 9 that the crest height of the largest waves is not necessarily increased, when wind is present. However, the lowest crest heights of the top 500 waves are increased i.e. the lowest part of the point cloud is moved upwards, which is especially pronounced for sea state B and D. To get a quantitative measure of how much the point cloud is moved, when the wind is introduced, the Mahalanobis distance [24] is found for the point cloud of 5.5 m/s with the point cloud of 0.0 m/s as reference. The mean of these distances is found in table 4. Since the mean of the distances is largest for sea state B and D, the point cloud is altered the most here, when introducing wind. This confirms the previous observation that the averages are moved the most upwards for sea state B and D. The power spectrum of the waves, shown in figure 9, indicates that the wind seems to steepen the waves more specific there is more energy at the right hand side of the frequency peak. It is challenging to explore exclusively the direct effect of an instantaneous wind field above the waves, since the indirect effect of wind will inevitably accompany. This means that short wind-generated waves and small ripples are generated and mixed with the wave paddle signal. These short waves will appear around frequencies of wave spectrum, and they are somewhat different from those purely generated by the wave-paddles. Moreover, it is found that the spectrum of the wave gauge signal, measured right in front of the pile, has the same peak frequency and distribution as the input signal to the wave paddles. It was observed in measurements from all four wave gauges in the tests without wind that the significant wave height was decreasing throughout the tank, probably due to breaking dissipation, viscous damping and water friction along the vertical walls [25],[26]. Therefore, it is useful to get a confirmation that the spectrum is nevertheless not altered significantly throughout the tank.

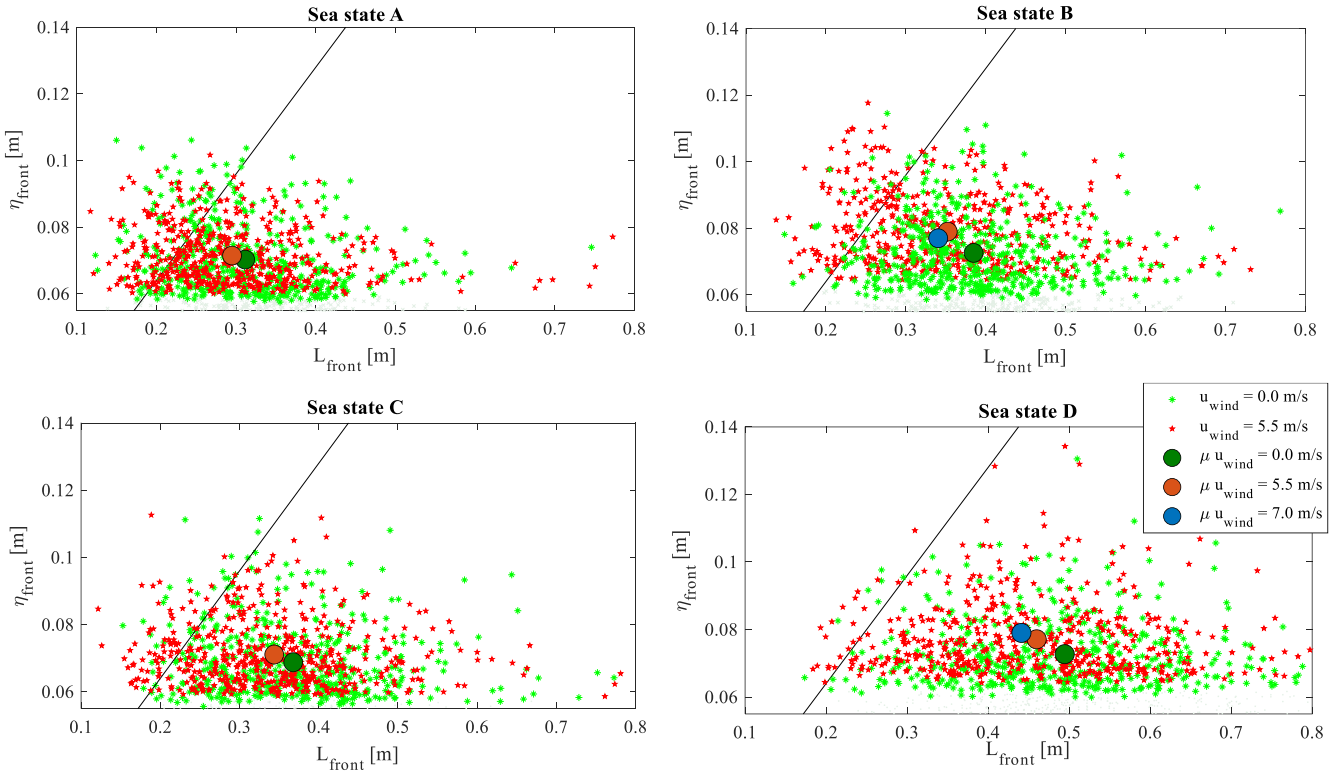

Figure 8: Crest height, η_{front} against length of the front of the wave, L_{front} for sea state A-D with wind velocity of 0.0 m/s and of 5.5 m/s for the largest 500 waves. The larger dot marked with dark green is the mean of the height and front length of top 500 waves for wind velocity of 0.0 m/s, whereas the large, red dot is for 5.5 m/s and the larger, blue dot is for 7.0 m/s. The black line marks the breaking limit of Kjeldsens, where the dots to the left of the line break.

Table 4: The number of the first column is the Mahalanobis distance for the point cloud of wind velocity 5.5 m/s with the point cloud of wind velocity 0.0 m/s as reference, whereas the third column is for the point cloud of wind velocity 7.0 m/s with the point cloud of wind velocity 5.5 m/s as reference. Change of mean of crest height and of length of front of waves in percentage, when going from 0.0 m/s to 5.5 m/s in second column and from 5.5 to 7.0 in fourth column.

Sea state	Mahal($[\eta_0, \lambda_0],[\eta_{55}, \lambda_{55}]$)	$\lvert\mu[\lambda_{55}, \eta_{55}]-\mu[\lambda_0, \eta_0]\rvert/\mu[\lambda_0,\eta_0]$)	Mahal($[\eta_{55}, \lambda_{55}],[\eta_7, \lambda_7]$)	$\lvert\mu[\lambda_7, \eta_7]-\mu[\lambda_{55}, \eta_{55}]\rvert/\mu[\lambda_{55},\eta_{55}]$)
A	1.8673	[-0.0530, 0.0171]		
B	2.3934	[-0.0842, 0.0882]	2.3700	[-0.0338, -0.0253]
C	1.8653	[-0.0653, 0.0190]		
D	2.3214	[-0.0761, 0.0605]	2.0443	[-0.0433, 0.0246]

4.2 Effect of wind on the number of breaking waves

Kjeldsen's breaking criterion [23] is for all sea states applied on the front steepness of the waves, ϵ, which definition is shown in figure 8. This is done in order to explore the estimated number of breaking waves for the different wind conditions. The waves to the left of the line in figure 10 is according to the applied breaking criterion counted in as breaking, and those events are summarized and tabulated in table 5 sketched in figure 11. The number of waves with crest height above 0.06 m exceeding the breaking limit is also listed to obtain an estimate of the number of breaking waves of a considerable height. The application of this breaking criterion shows that the number of breaking waves in all sea states is increased with the introduction of wind. The severity is decreasing from sea state A to D, and the number of breaking waves follows that trend, i.e. there is a larger number of breaking waves in sea state A than in sea state D. The larger severity of sea state A without wind, results in a smaller percentage increase in number of breaking waves, when wind is introduced, because a substantial part of the waves are already breaking. The percentage increased by a factor of 1.60. A larger increase in number of breaking waves was experienced for sea states B and C, which both increased by a factor of 2.27, when wind increased from 0.0 m/s to 5.5 m/s. The largest increase factor for number of breaking waves was 2.74 and was experienced for sea state D, when the wind velocity was increasing from 0.0 to 5.5 m/s. An increase in breaking waves when increasing wind velocity from 5.5 m/s to 7.0 m/s is present for sea state B and D by a factor of 1.42 and 1.63, respectively. The percentage increase was hereby smaller when the wind velocity increased from 5.5 to 7.0 than when it was going from 0.0 m/s to 5.5 m/s. The picture is slightly different if we only observe the waves of a certain crest height, namely those larger than 0.06 m. When the wind velocity is increased from 0.0 m/s to 5.5 m/s, the number of breaking waves having a crest height larger than 0.06 m increased with a factor 1.32, 2.12, 1.77 and 1.56 for sea state A, B, C and D, respectively. The largest increase experienced for sea state B, could mean that the steepness of the highest waves is large enough to enable energy transfer from wind to the waves, but still so small that the waves are not already breaking before the wind is interfering. The latter being an interpretation of what occurs for sea state A, where the smallest increase in the number of waves is observed.

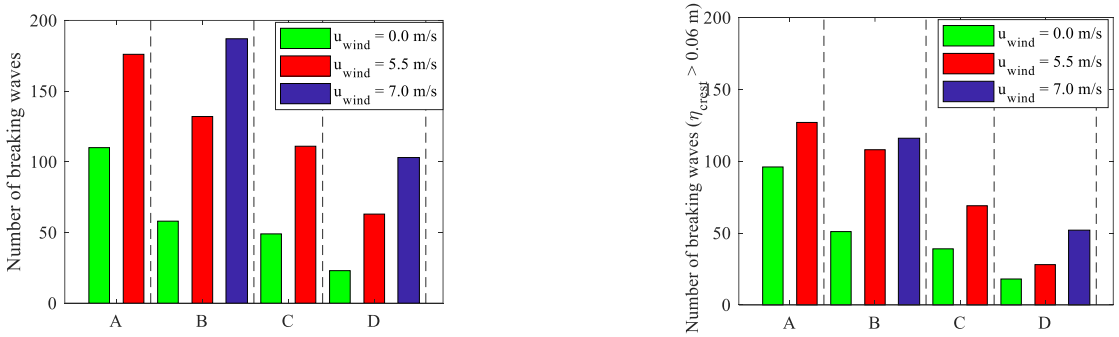

Figure 9: Bar plot of number of breaking waves in sea state A, B, C and D for different wind velocities. Left plot is for all waves, whereas right plot is only of the waves having a crest height larger than 0.06 m.

Table 5: Number of breaking waves estimated with Kjeldsens breaking criterion for sea state A-D with wind velocity of 0.0, 5.5 and 7.0 m/s.

Sea state	A			B			C			D		
Wind velocity [m/s]	0.0	5.5	7.0	0.0	5.5	7.0	0.0	5.5	7.0	0.0	5.5	7.0
Number of breaking waves	110	176	-	58	132	187	49	111	-	23	63	103
Number of breaking waves, η_{crest} >0.06 m	96	127	-	51	108	116	39	69	-	18	28	52

4.3 Effect of wind on statistics of wave-induced load, total force and front line pressure

The spectra of the force signals measured with the load cells is shown in figure 12. The spectrum is plotted in the frequency range 0-100 Hz and beside is zoomed in on the frequency range 0-3 Hz. There is increased energy at the natural frequencies of the structure at 65.7, 81.2 and 89.5 Hz when the wind velocity is increased from 0.0 m/s to 5.5 m/s for all sea states. This means that the dynamic loading is largest for the tests with wind, which points at more steep and breaking waves, which enables slamming and high impulsive loading. There is smaller variations between the case with and without wind in the frequency range 0-3 Hz.

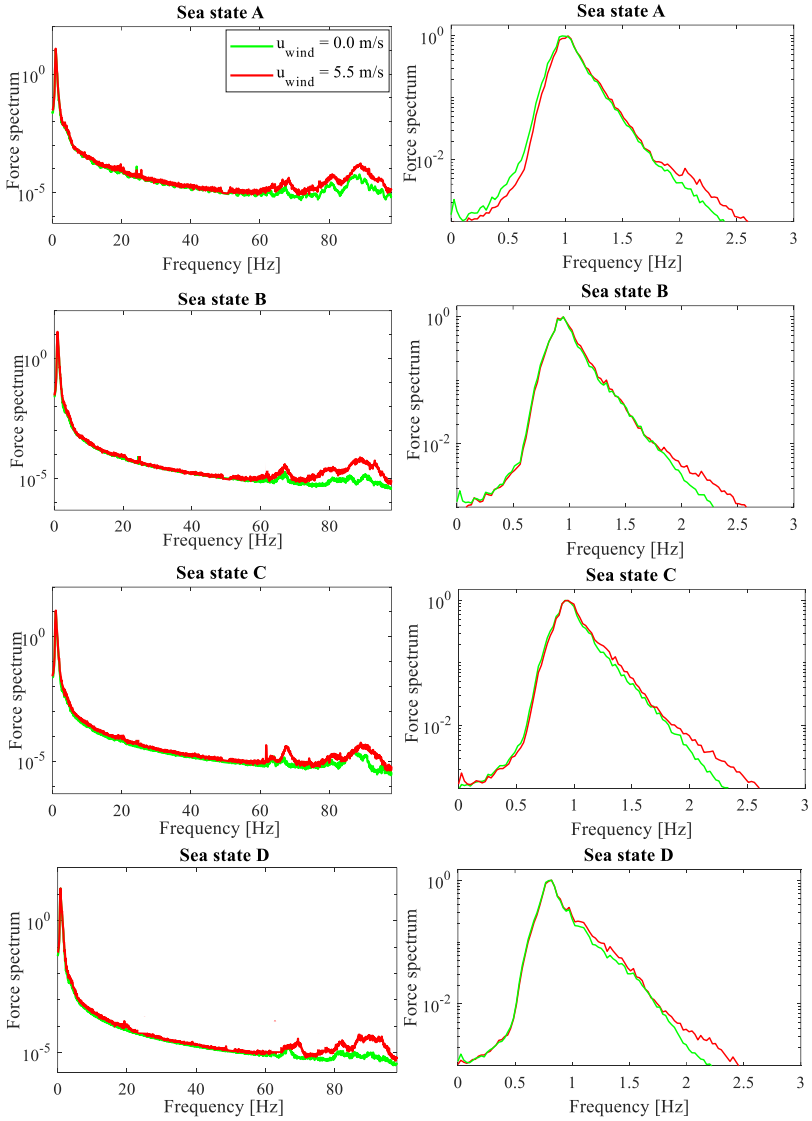

Figure 10: Power spectrum of force signal for sea state A-D with wind velocity 0.0 and 5.5 m/s. The top plots are in the frequency range [0-100] Hz and the bottom plot is in the range [0-3] Hz. The green line is for tests with wind velocity of 0.0 m/s and the red is of 5.5 m/s.

The focus is now on the peak statistics of surface elevation, inline force and pressure. The force signal was however, first low pass filtered up to 45.0 Hz, since the first natural frequency of the model is found at 65.6 Hz, whereas the peak of the wave loading is identified as the first peak. The load and pressure peaks were found in-between all zero-down-crossings performed on the signal of wave gauge 3. The wave-induced load and the total force were sorted in ascending order, and plotted in figure 13 against exceedance probabilities found as P=1-(i-1) /N, i=1,2…N. The crest height of waves in sea state A is affected of wind for exceedance probabilities, p_{exc} smaller than $1 \cdot 10^{-2}$ since their increase in crest height in this region is lower than for the events without wind (see figure 13a). Since the sea state is severe, this could indicate an earlier initiation of breaking for waves with wind above. In figure 13b, the force is presented as a low-pass filtered version corresponding to the wave-induced load, and as a force, which contains energy of all frequencies in the frequency band 0-800 Hz. The latter is interpreted as a total force containing both wave-induced load and dynamic loading, whenever the natural frequencies of the model is excited.

The wave-induced load events of sea state A has a high similarity in the exceedance probability curves, whether wind is present or not. For $p_{exc} < 5 \cdot 10^{-4}$ the wave-induced load shows smaller peak values when wind is introduced. The total force is on the other hand enlarged by the wind for $p_{exc} < 3 \cdot 10^{-3}$. The front face pressure show a clear wind-induced increase for $p_{exc} < 1 \cdot 10^{-2}$. The 10,000-years pressure value is increased with a factor 1.73. These observations can be linked to the increased amount of breaking waves (see table 5), which expectedly exerts a larger amount of slamming type impacts on the structure. The trend is clear for the pressure and total force, which is impacted through structural vibrations at the natural frequency of the model. The slamming loads seems however to be too localized in space and time to affect the wave-induced load. Despite an increase in the amount of breaking waves, the extreme events of the wave-induced load experience a small reduction, which might be due to smaller crest height of the waves. Nonetheless, if breaking waves have smaller crest heights compared to larger ones of non-breaking waves, the wave-induced load might not be enlarged by the slamming of the breaking waves.

The exceedance probability curve for the crest height of sea state B (see figure 13a) exhibits changes, when wind is present. For one thing, the crest height is slightly increased in the range of exceedance probabilities from $2 \cdot 10^{-2}$-$5 \cdot 10^{-1}$, and as for another, it is lower than the events occurring without wind for $p_{exc} < 5 \cdot 10^{-3}$. The wave-induced load is correspondingly increased in the first-mentioned range (see figure 13b). The wave-induced load begins on the other hand to increase significantly in the last-mentioned region, which points towards initiation of breaking. The 10,000-years wave-induced load is increased by a factor 1.3 and 1.4, when the wind velocity is respectively 5.5 m/s and 7.0 m/s compared to 0.0 m/s. The total force in test with wind velocity of 5.5 m/s and 7.0 m/s is increasing abruptly for $p_{exc.} < 5 \cdot 10^{-3}$ and is increased by a factor of 1.6. The abruptly increase in the tail due to wind is even more pronounced for the pressure events (see figure 13c). The 10,000-years pressure event is increased with a factor 2.1 and 4.3 for wind velocity of respectively 5.5 m/s and 7.0 m/s compared to 0.0 m/s. This sea state is less severe than sea state A, so the smaller exceedance probability, at which breaking initiation is assumed, corresponds well to a lower number of breaking waves in this sea state than in A. Due to a larger crest height of the steepest waves as seen in figure 10, the tail of the exceedance probability curve for this sea state is therefore increased for both the wave-induced load, the pressure and the total force, when wind is introduced.

A conclusion for the less severe sea state C is more difficult to draw, since the changes, when wind is introduced, are minor. The crest height is only experiencing a small drop in the tail of the exceedance probability curve for the case with wind compared to the case without wind. The same observations as for sea state A applies for the wave-induced load, total force and front line pressure except from a couple of the most extreme total force and pressure events. Here the case without wind nevertheless experiences a larger increase (see figure 13b+13c). These events are however, extreme even compared to the events of sea state B without wind, which otherwise are expected to be more extreme. The general picture is however, that slamming-type impacts are more frequently, when wind is present, which is consistent with the observations on number of breaking waves determined with a breaking criterion.

Mainly, the same conclusions as for sea state B apply to sea state D, which has the lowest severity of the four sea states. The tail of the exceedance probability curve for crest height (see figure 13a) starts to decline abruptly at $p_{exc} < 1 \cdot 10^{-3}$, at which point and on, the wave-induced load is slightly increased in the cases with wind. The largest increase of the 10,000-years wave-induced load is of a factor 1.13, which is nonetheless achieved for the second highest wind velocity of 5.5 m/s. The total force for both wind velocity of 5.5 m/s and 7.0 m/s is increased considerably at $p_{exc} < 2 \cdot 10^{-3}$ and results in an increase in the 10,000 years force of respectively 1.4 and 1.3 compared to the case without wind. The 10.000 years pressure event is increased by a factor 1.5 and 4.1 for an event with a wind velocity of respectively 5.5 m/s and 7.0 m/s. A couple of more extreme events of wave-induced

load and total force are nevertheless experienced for the case with wind velocity of 5.5 m/s than for the case of highest wind velocity of 7.0 m/s. This could be explained with larger crest height of the waves generating the load, or that the wave front is more unstable for the highest wind velocity and thereby not uniformly breaking. The latter point is observed in videos of focused wave with a wind velocity of 7.0 m/s. The total force is not increased as significantly as for sea state B, which could be due to the lower steepness of the waves, which is a crucial factor for the occurrence of airflow separation and thereby energy transfer from the wind to the waves.

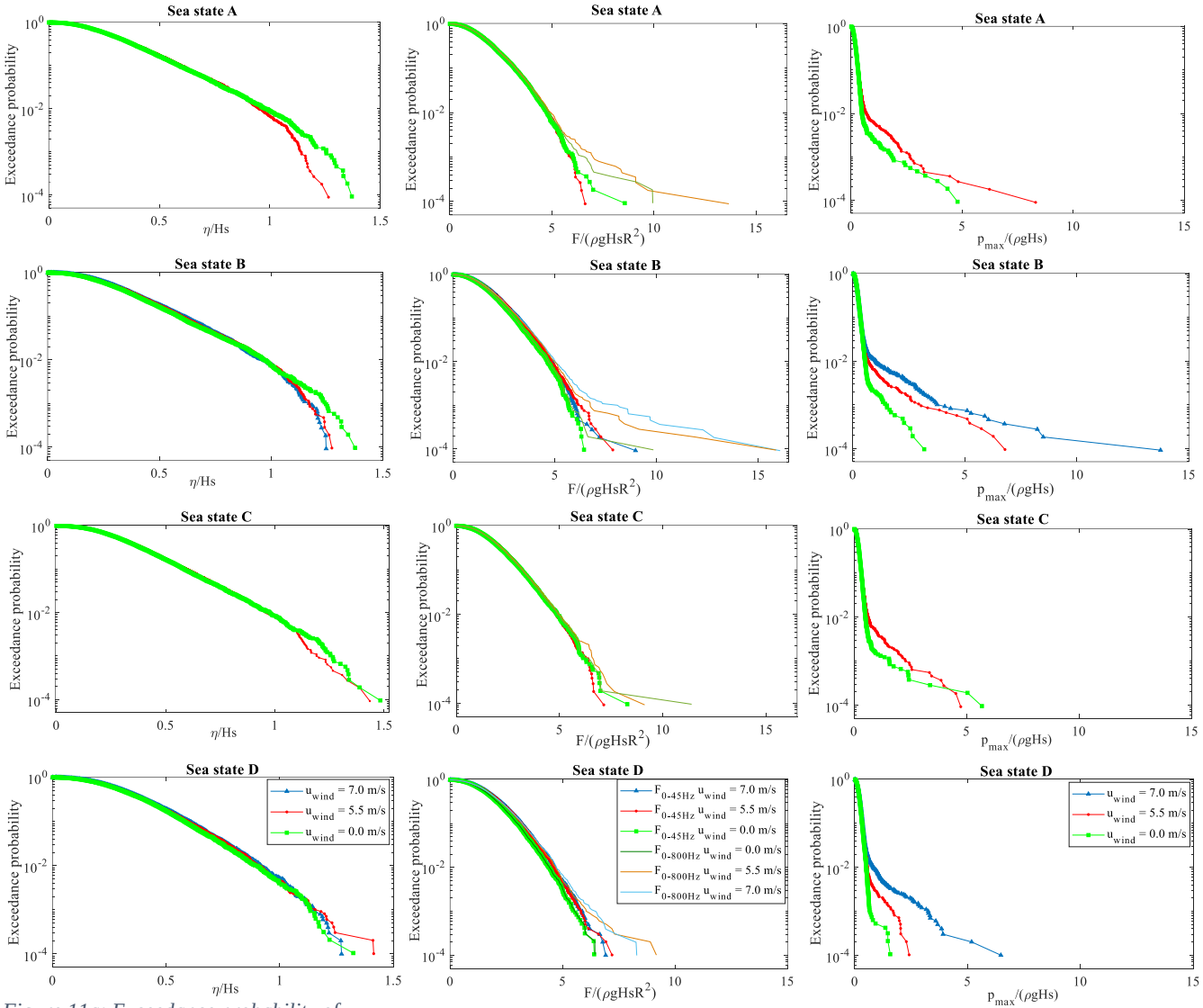

Figure 11a: Exceedance probability of normalized crest height, η.

Figure 13b:Exceedance probability of normalized wave-induced load, $F_{0\text{-}45Hz}$ and total force, $F_{0\text{-}800Hz}$.

Figure 13c: Exceedance probability of normalized pressure, p.

Since the events in the tail of the exceedance probability curve are associated with large variations, we constructed an exceedance probability curve of the crest height, wave-induced load and pressure events averaged over 10 tests at every exceedance probability from 10^{-3} to 1. The standard deviation of the events over ten tests is calculated as well. The curves with the mean and standard deviation of the crest height, wave-induced load and pressure for sea state A-D with and without wind are plotted respectively in figure 14a, 14b and 14c. There is a good repeatability

for crest height and wave induced load. The standard deviation is however increasing with decreasing exceedance probabilities, which also confirms the large statistical variations of the largest wave induced load events with slamming involved. The standard deviation of the wave-induced load for sea state B and D is in the tail larger for wind velocity of 5.5 m/s and 7.0 m/s than 0.0 m/s, which is consistent with an increased amount of breaking waves of considerable height. The standard deviation of wave induced load is for sea state A and C on the contrary largest for the cases without wind, which suggests a large number of slamming-type impact from waves of large crest height. At the lowest level of p_{exc} of 10^{-3} σ/μ is typically in the range 0.03-0.06 for crest height and in the range 0.06-0.16 for wave-induced load. The mean of the force for sea state B is in tests with wind coinciding with the mean plus the standard deviation of the force for tests without wind when $p_{exc} < 5 \cdot 10^{-3}$. If assuming that the mean of the 1,000 years wave-induced load without wind is following a Student's t-distribution with 10 samples, a 68 % confidence interval of it, will not exceed the mean in the case with wind.

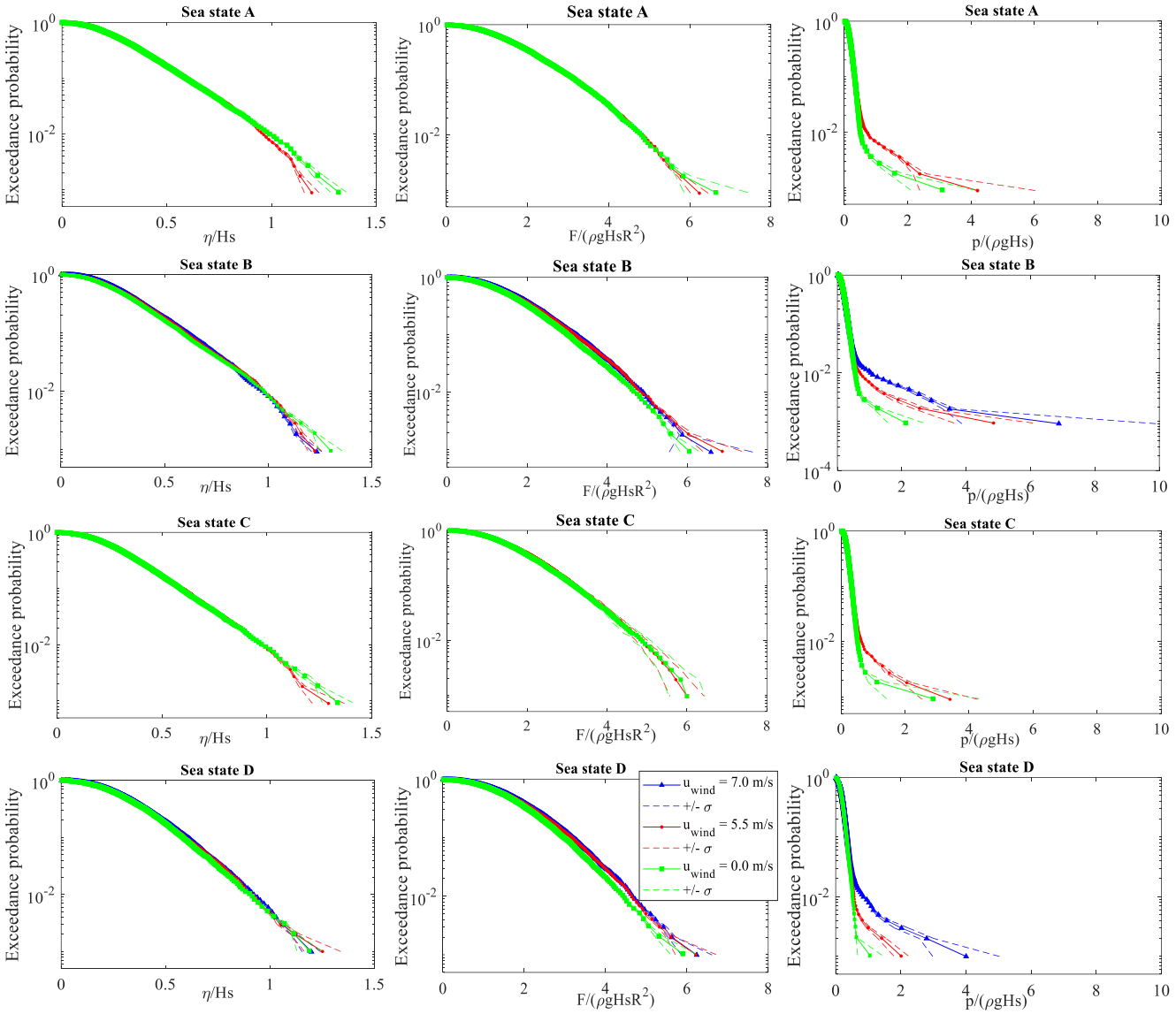

Figure 12a: Exceedance probability curve for mean and standard deviation of crest height measured in ten independent tests

Figure 14b: Exceedance probability curve for mean and standard deviation of force measured in ten independent tests

Figure 14c: Exceedance probability curve for mean and standard deviation of pressure measured in ten independent tests

The front line pressure shows larger stochastic variability at $p_{exc} = 10^{-3}$. Still, the trend of wind effect is clearly detectable from $p_{exc} < 1 \cdot 10^{-2}$. The 1,000 years wave induced pressure is for sea state A increased with a factor 1.4 when the wind velocity is increased from 0.0 to 5.5 m/s. For sea state B it is increased by a factor of 2.3 and 3.3, when increasing the wind velocity from 0.0 m/s to respectively 5.5 m/s and 7.0 m/s. It is notable that the 1.000-years pressure event is still increased with a significant factor – in fact a larger factor than the 10.000 year value, when increasing the wind velocity. The 1,000 years wave-induced pressure is for sea state D increased by a factor of 1.9 and 3.8, when increasing the wind velocity from 0.0 m/s to respectively 5.5 m/s and 7.0 m/s. Another interesting observation is done for the 1,000 years pressure of sea state C, which is by a factor of 1.2 larger for the case with wind than without wind, which is opposite to what was observed for the 10,000 years pressure. For $p_{exc} < 8 \cdot 10^{-3}$ the mean of pressure in tests with wind is more than one standard deviation larger than the case without

wind. This supports the conclusion from the above-mentioned exceedance probability plots for sea state C, that even though the wave-induced load is not altered with the introduction of wind, the pressure is significantly increased due to the slamming effects from the increased number of breaking waves. Although the extreme slamming pressure show larger variability than the force, the wind effect is clearly detectable for all sea states.

4.4 Effect of wind on pressure profiles

We now turn to the wind effect on the pressure profiles over the depth. The pressure profile of the ten largest pressure events is plotted in figure 15, to explore if they explain why the events in the tail of the exceedance probability curve is increased, when wind is introduced, whereas the wave-induced load is not increased for all sea states. For sea state B and D, where both the wave-induced load and the pressure are increased, the profiles are similar from 0.03 m above the mean water level and down, but from that point and higher the pressure is increasing with increasing wind velocity. For these extreme pressure events, the very high pressures are reached at 0.09 m above the mean water level for all wind velocities. For sea state A, the maximum pressure is reached at 0.03 m for the tests with wind velocity of 5.5 m/s. The lower maximum value of pressure in tests without wind is on the other hand reached at an elevation of 0.09 m. The same applies to the profiles in sea state C except that here the largest maximum pressure is reached in the tests without wind. These plots confirm that the steep and breaking waves of sea state A and C with wind are not targeting the model as high as in the tests without wind, and thereby not giving as large depth-integrated forces. It is also consistent with the distribution in figure 10, where there are few of the steepest waves in the high crest height region, when wind is introduced.

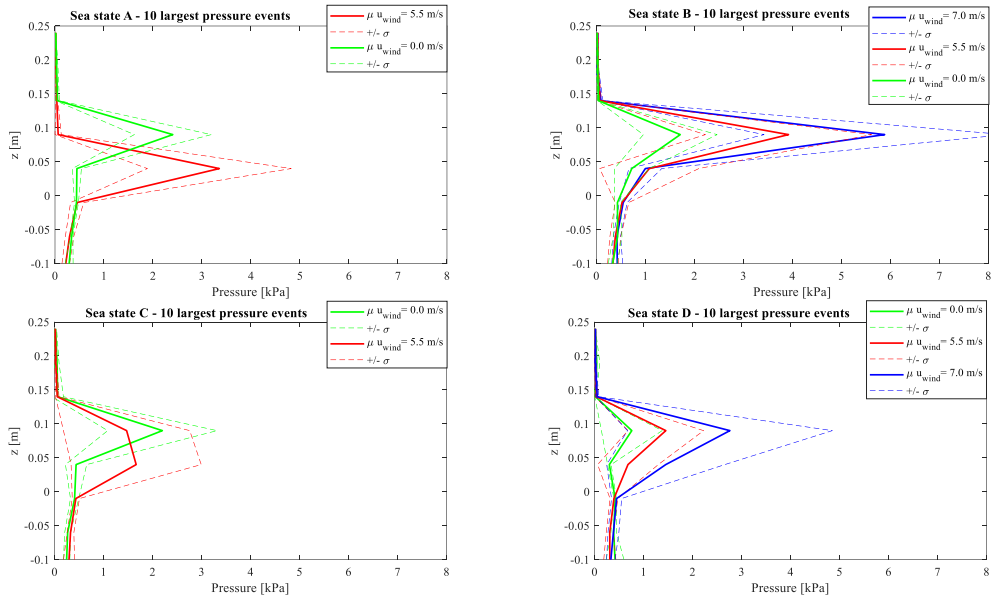

Figure 13: Plot of pressure profile averaged for the ten largest pressure events experienced for all sea states at all tested wind velocities. The standard deviation around the mean is marked with a dashed line. The z-axis is defined with 0.0 m corresponding to the mean water level.

5. Average shape of the hundred largest force events

The largest events in the force statistics for different wind velocities are investigated more comprehensively by looking at the force and wave shape around the force peak averaged over the 100 highest wave events in terms of crest height. This evaluation is performed in order to get a behavioral description of the apparent change in the force statistic caused by wind. The average shape of the ten largest force events of sea state B for wind velocity of 0.0, 5.5 and 7.0 m/s is plotted in figure 16. The most probable force shape determined by the New Force model defined in section 2.1 is plotted with the black dashed line. The maximum value of the New Force shape is scaled corresponding to the peak of the case without wind. The New Force, $F_{NF}^{(1)}$ therefore fits the peak of the green line corresponding to wind velocity of 0.0 m/s, whereas the trough of the force both before and after the peak is overestimated with New Force. When the second order force components are added, $F_{NF}^{(1)} + F_M^{(2)}$ the fit is improved in the trough. The second order force describes the preceding force crest less accurate than the crest after the peak especially for the cases with wind. A possible explanation could be that the preceding wave has already broken before it reaches the model and thereby energy is dissipated, and the suction generated of the motion on the rear side of the wave is less energetic. The second order surface elevation, $\eta_{NF}^{(1)+(2)}$ derived from the second order force is nearly coinciding with the measured surface elevation without wind except from some deviations on the rear side of the primary wave and on the preceding wave (see figure 17). The latter is nevertheless expected since the force of the preceding wave is poorly described as well. The averaged force peak of the cases with wind contains an additional spiky top, which can be explained with the impulsive force shape generated by breaking waves. This is interpreted in the way that the ten largest force events for the tests with wind mainly are generated by extreme breaking wave events opposite to the case without wind, which does not have a spiky peak. The averaged surface elevation of the primary wave has in addition a steeper wave front for the cases with wind, which confirms that these are close to or at breaking. This behavior supports the observation that the extremes of the force statistics are more violent for the cases with wind in sea state B.

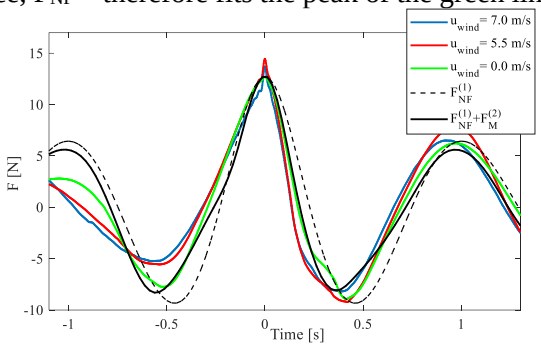

Figure 14: Average force shape of the ten largest force events of sea state B for wind velocity of 0.0, 5.5 and 7.0 m/s. First and second order New Force Model is plotted in black dashed and full line, respectively.

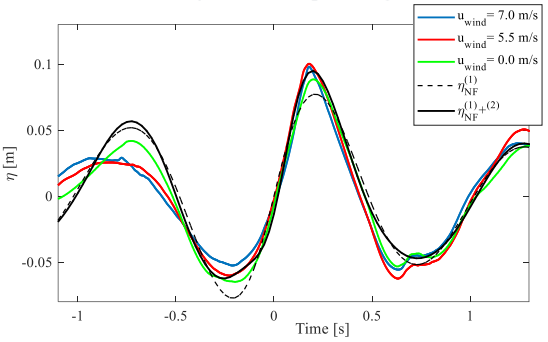

Figure 15: Average wave shape corresponding to the ten largest force events of sea state B for wind velocity of 0.0, 5.5 and 7.0 m/s. First and second order surface elevation derived of New Force Model is plotted in black dashed and full line, respectively.

The force – and wave shape of sea state A, B, C and D of the hundred largest wave-induced load events are plotted in figure 18 for the different wind velocities. For sea state A, there is hardly no difference in force- or wave shape whether a wind field above the waves is present or not. For both tests with and without wind an additional spike is observed at the maximum of the 100 averaged force events, which indicate a high number of breaking waves for both cases. For sea state B, the effect of the wind on the averaged force shape is an addition of a spike on the peak of the force, which is characteristic for breaking waves. The surface elevation for the cases with wind of sea state B is also steeper and close to breaking opposite to the case without wind. Both the alteration in force and surface elevation is consistent with the observation that the direct effect of wind increases the number of breaking waves. For sea state C there is no recognizable effect of wind, and there is no spike on the peak of the averaged force shape for neither tests with wind velocity of 0.0 m/s nor for those with 5.5 m/s, which indicates a low number

of breaking waves among the waves of the top hundred largest force events. For sea state D, the cases with wind achieves a small spike on the primary force crest. This small spike is not present for the case without wind, which supports the conclusion, that a higher number of waves are breaking in this sea state when the wind velocity is introduced.

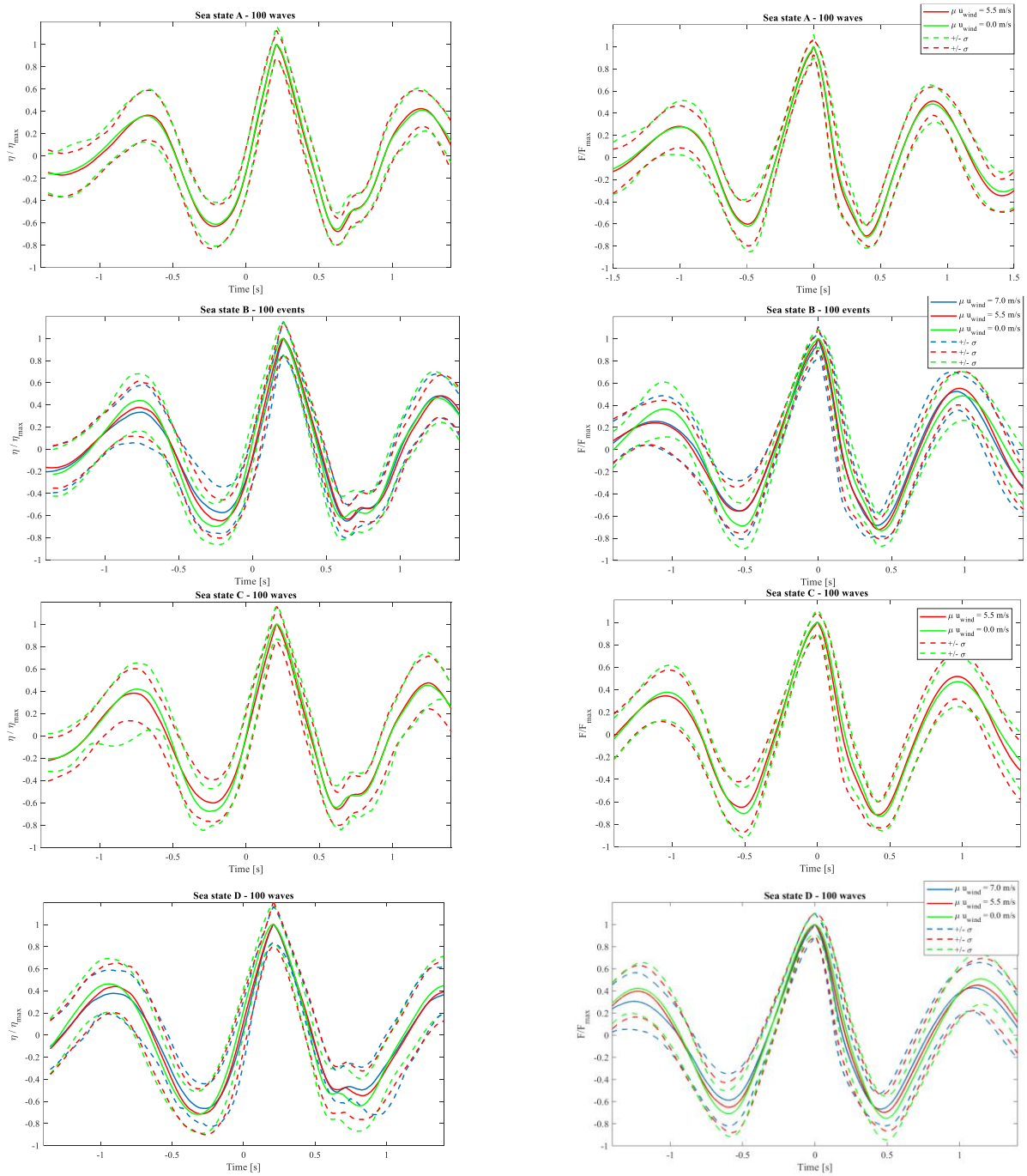

Figure 16: Normalized force – and wave shape of the hundred largest force events for all sea states with the tested wind velocities

6. Phase-based harmonic separation of force

To explore the wind's effect on the harmonic components of the force from first to fourth order, a phase-based harmonic separation method is applied on four phase-shifted time series of irregular waves of sea state B with wind velocity of 0.0 m/s and 5.5 m/s. The harmonic force components over the entire time series of irregular waves are estimated. Since the majority of these waves contains a rather small amount of high-order force components, only the components of the 25 largest force events are selected for further study. The 25 largest force events are selected based on the summation of all force component. All 25 force time stories of $F^{(1)}$ are centered at the peak and averaged. The higher order force components $F^{(2)}$, $F^{(3)}$ and $F^{(4)}$ are shifted corresponding to $F^{(1)}$ and then averaged. The estimated harmonic force components for a case with wind velocity of 0.0 m/s and 5.5 m/s are plotted in figure 19 in top and bottom plots, respectively. The forces are normalized with the sum of all components, F_{total}. The second order component is as expected located with a trough on the left side and a crest on the right side of the peak of the first order component. The plots also show how the harmonic force content decreases as the order increases. A change in the case with wind is that the peak of the total force occurs more to the right of the first order peak. This indicates that the higher order force components are of greater influence in the case with wind. The separated force components are as well plotted in the frequency domain in figure 20. Despite the noise in the spectra of the higher order, the peak of the second, third and fourth order spectrum is as expected identified at a frequency of respectively a factor of 2, 3 and 4 multiplied with the peak frequency of the first order spectrum. Additionally, it is confirmed that the spectrum of the fourth order contains the content of the second order subharmonic with the main energy located at frequencies lower than the peak frequency of the first order spectrum. There is a tendency to wider spectra when wind is present, especially for those of second and third order. To enable the comparison between the force components for wind velocity of 0.0 m/s and 5.5 m/s, each component is presented in a single plot in figure 21a-d. The force is not normalized in these plots. The peak of the first order component is coinciding for the case with and that without wind. Both the second and third order component contains more energy especially around the first order peak for the case with wind, whereas the content of the fourth order is overall slightly reduced with wind. To get a quantitative measure, the non-dimensional Stoke-type force coefficients are found as in [27], [28], [29] and is shown in figure 22. The force coefficients are found $\widetilde{F_n} = \widehat{F_n} / \left(\rho g \pi R^2 C_F A (Ak_p)^{(n-1)}\right)$ where ρ is the density of water, g is the

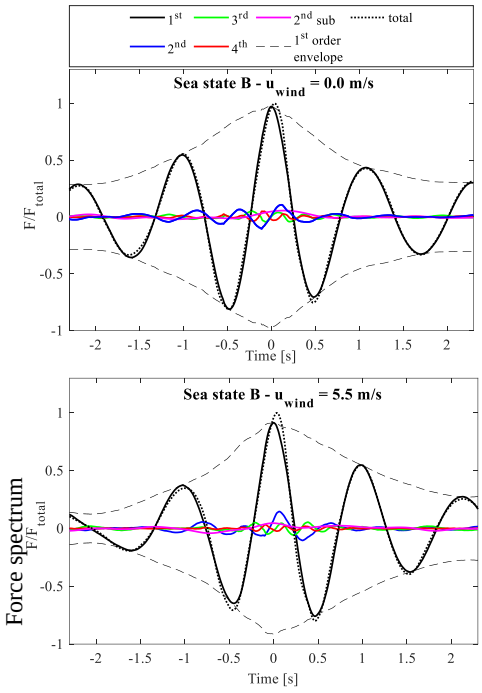

Figure 17: Normalized harmonic force components from first to fourth order estimated by the phase-based method [2] for wind velocity of a) 0.0 and b) 5.5 m/s in respectively top and bottom plots for sea state B. The first order envelope is the thin dashed line. The dotted line is the sum of all components.

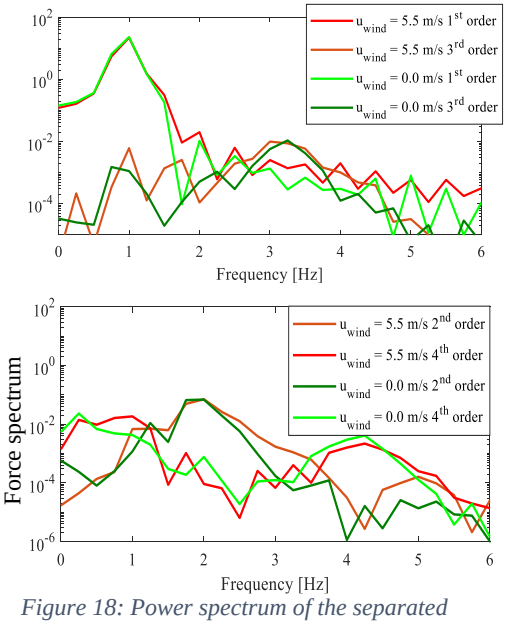

Figure 18: Power spectrum of the separated harmonic force components from first to fourth order estimated by the phase-based method [2] for wind velocity of a) 0.0 and b) 5.5 m/s in respectively top and bottom plots.

acceleration of gravity, R is the radius of the cylinder, A is the maximum of the wave amplitude, k_p is the peak wave number and n is the harmonic order. $\widehat{F_n} = \max(\sqrt{F_n^2 + (F_n^H)^2}$. There is a clear tendency towards an increase in the force coefficients, when the wind is increased for both sea state B and D. The second order harmonic force coefficient is however slightly decreased for sea state B, when the wind velocity is increased from 0.0 m/s to 5.5 m/s, whereas the largest second order force coefficient is appearing for wind velocity of 7.0 m/s. The entire phase based separation approach is, however, very sensitive to the degree of success of obtaining exactly 90, 180 and 270 degrees phase shift between the force time series. This is difficult to achieve, when the waves are travelling a long distance of 29.4 m down the flume. Naturally, high repeatability is a key factor in obtaining reliable estimates with the method, and this is not investigated in greater depth. The phase shift of the time series is slightly adjusted based on optimization of highest correlation. Despite this adjustment, the method has of aforementioned reasons high uncertainty for these tests.

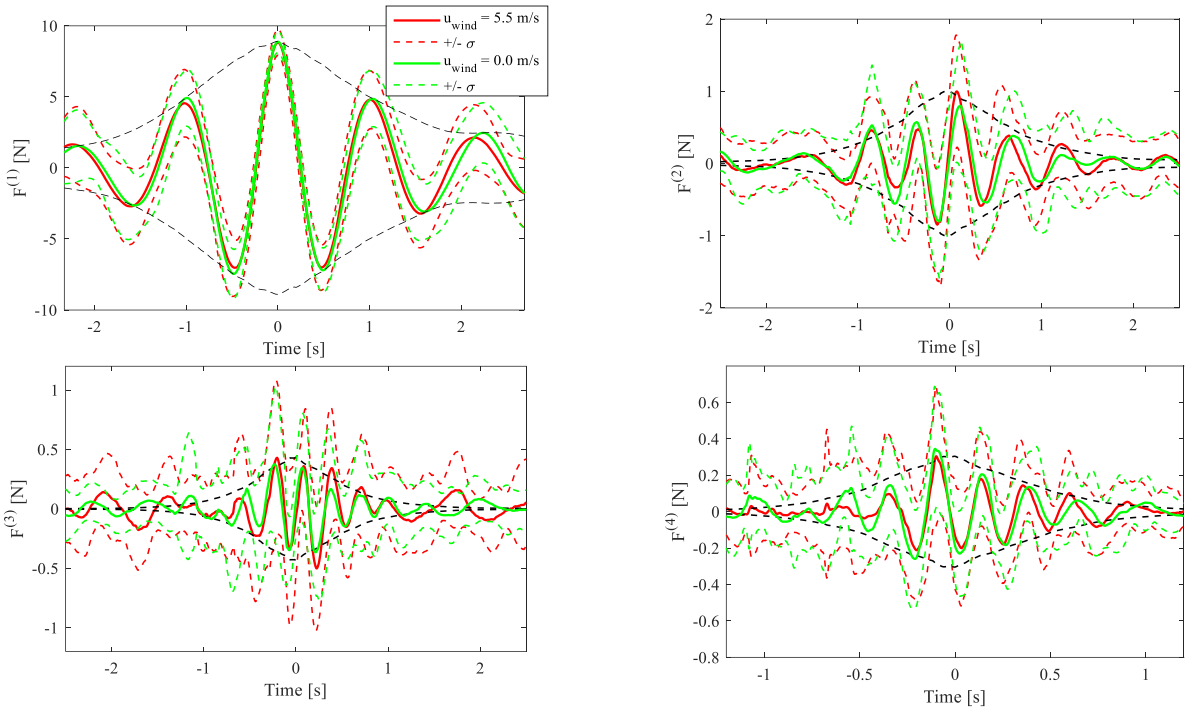

Figure 19a-d: First to fourth order force components estimated with the phase-based harmonic separation method. The data is from sea state B for wind velocity of 0.0 m/s (green line) and 5.5 m/s (red line). The black line in plot b, c and d are the first order envelope for the case with wind respectively squared, cubed and quad.

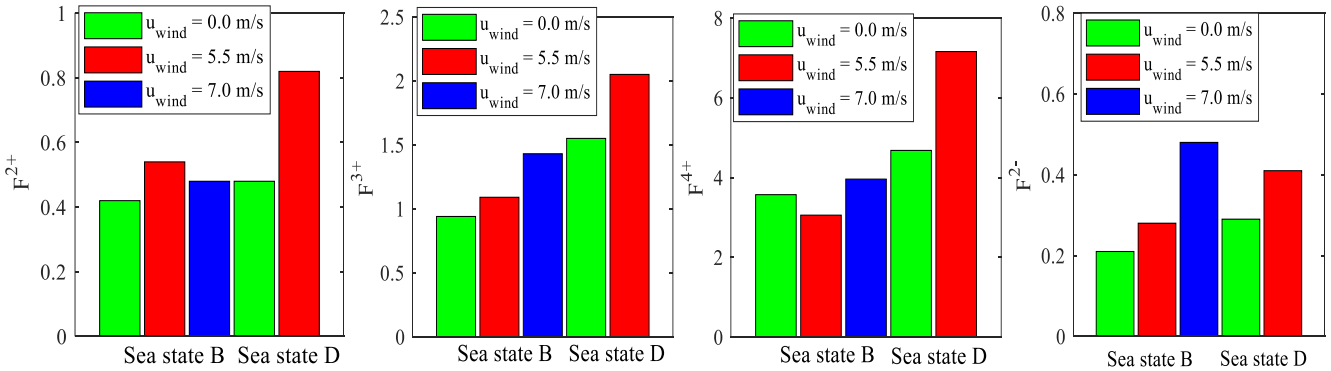

Figure 20: Force coefficients of 2nd to 4th order super harmonic and 2nd sub harmonic force of sea state B and D with wind velocity 0.0, 5.5 and 7.0 m/s. Tests are not existing for sea state D with wind velocity of 7.0 m/s

5. Summary and conclusions

A set of tests with irregular waves introducing wave loading on a cylindrical model were performed both with and without wind, however with the same significant wave height within one sea state measured right before the model. The direct effect of the wind on both the wave field, the statistics of the wave-induced force and pressure is explored. When wind is introduced above irregular waves of the investigated sea states, the crest heights of lowest exceedance probabilities are decreased compared to the case without wind. Another effect of introducing wind above the waves is an overall increase in the steepness of the wave field and in the number of waves characterized as breaking. Nevertheless, these differences in tests with and without wind are not converted to an increase in the wave-induced load statistics. Only in two out of the four investigated sea states, the 10,000 years wave-induced load is increased, when increasing the wind velocity. A possible reason why the wave-induced load is not increased for all sea states, could be that the sea state is already saturated in terms of large breaking waves in the tests without wind. A significant increase is however, present for the extreme events of the wave-induced pressure and of the total force in all sea states, when the wind velocity is increased. The 10,000 years pressure and total force event is increased by up to a factor of respectively 4.3 and 1.6. When averaging over ten realization tests, it enables an exceedance probability curve with less statistical scatter. Here an increase by up to a factor of 3.8 in the 1,000 years pressure from a wave event with wind is discovered. The same trends applies, when the wind velocity is increased from 5.5 m/s to 7.0 m/s. The wave-induced load and total force is not further increased at a wind velocity of 7.0 m/s, and a possibly explanation could be that a saturation for breaking of the largest waves in terms of crest height is reached already at a wind velocity about 5.5 m/s. The wave-induced pressure is further increased when increasing the wind velocity from 5.5 m/s to 7.0 m/s. With the introduction of wind, another interesting feature regarding the front line pressure is revealed. The largest pressure over the height is namely experienced at a pressure sensor located 0.07 m below the one experiencing the largest pressure, when no wind is present. A possibly explanation is that breaking is initiated for the case with wind, and the overturning crest is targeting the model at a lower height than when the wave is not breaking.

The features of the direct effect of wind are explored by inspecting the average shape of the hundred largest force events of all sea states. Especially for the sea state B an additional spike is seen on the largest force crest, which confirms a larger number of slamming-type impacts, when wind is present.

The direct effect of wind on the harmonic components of the force up to fourth order is investigated as well. The shape of the second, third and fourth order force components both with and without wind are appropriately following the first order envelope squared, cubed and quad, respectively. The second and third order force components are in general increased with the introduction of wind. Moreover, it should be pointed out that they are increased around the peak of the first order component, which is what influences the force peak. The fourth order harmonic component is on the contrary decreased both in general and around the peak of the first order component, when wind is introduced.

It is essential that the increase in the steepness of waves and in the number of breaking waves in some cases lead to an increase in the wave-induced load statistics. More importantly, it does in all cases of this campaign lead to an increase in the statistics of the dynamic force due to the slamming of the steeper waves. This change of exceedance probability curve for the total force and the in-line force will be investigated in a future study by means of the potential solver program, OceanWave3D and of slender-body force model. Moreover, when designing joints and elements the increased wave-induced pressure statistics is a serious concern. If it should be incorporated into design codes, it requires more experimental and numerical investigations in order to formulate and calibrate engineering design models.

6. Acknowledgement

The authors acknowledge the funding received from Centre of Oil and Gas – DTU/Danish Hydrocarbon and Technology Centre (DHRTC). The help from technicians at the Department of Engineering at Aarhus University and at the Large Air Sea Interface Facility of Marseille University is very much appreciated. Moreover, a very helpful discussion and comments on the harmonic separation methodology and the interpretation of results with Paul Taylor and Thomas Adcock are appreciated.

7. References

[1] N. Reul, H. Branger, J. P. Giovanangeli, Air-flow separation above unsteady breaking waves, Physics of Fluids 11, 7 (1999) 1959-1961.
[2] V. Kudryavtsev, B. Chapron, V. Makin, Impact of wind waves on the air-sea fluxes: A coupled model, J. Geophys. Res. Oceans, 119 (2014) 1217– 1236.
[3] J.Touboul, J. P. Giovanangeli, C. Kharif, E. Pelinovsky, Freak waves under the action of wind: experiments and simulations, European Journal of Mechanics-B/Fluids 25(5) (2006) 662-676.
[4] N. Reul, H. Branger, J. P. Giovanangeli, Air flow structure over short-gravity breaking water waves, Boundary-layer meteorology 126(3) (2008) 477-505.
[5] S. Yan, Q. W. Ma, Numerical simulation of interaction between wind and 2D freak waves, European Journal of Mechanics-B/Fluids 29(1) (2010) 18-31.
[6] C.Kharif, J. P. Giovanangeli, J. Touboul, L. Grare, E. Pelinovsky, Influence of wind on extreme wave events: experimental and numerical approaches, Journal of Fluid Mechanics, 594 (2008) 209-247.
[7] P. Sullivan, J.C.Mc Williams, Dynamics of winds and currents coupled to surface waves, Annual Review of Fluid Mech. 142 (2010) 19-42.
[8] J. Chambarel, C. Kharif, & O. Kimmoun, Generation of two-dimensional steep water waves on finite depth with and without wind, European Journal of Mechanics-B/Fluids 29(2) (2010) 132-142.
[9] J. C. Kristoffersen, H. Bredmose, C. T. Georgakis, Preliminary numerical study on the influence of a wind field on wave-induced load on a circular cylinder, In *The 28th International Ocean and Polar Engineering Conference*. International Society of Offshore and Polar Engineers. (2018).
[10] A.P. Engsig-Karup, H. B. Bingham, and O. Lindberg, An efficient flexible-order model for 3D nonlinear water waves, Journal of Computational Physics. (2008). pp. 2110-2118.
[11] P. S. Tromans, A. R. Anaturk, P. Hagemeijer, A new model for the kinematics of large ocean waves-application as a design wave, In The 1st International Offshore and Polar Engineering Conference. International Society of Offshore and Polar Engineers (1991)
[12] S. Schløer, H. Bredmose, A. Ghadirian, Analysis of experimental data: The average shape of extreme wave forces on monopile foundations and the NewForce model, Energy Procedia 137 (2017) 223-237.
[13] J. R. Morison, J. W. Johnson, S. A. Schaaf, The force exerted by surface waves on piles, Journal of Petroleum Technology 2(05) (1950) 149-154.
[14] T. Kristiansen, O. M. Faltinsen, Higher harmonic wave loads on a vertical cylinder in finite water depth, Journal of Fluid Mechanics 833 (2017) 773-805.
[15] J. N. Sharma, R. G. Dean, Second-order directional seas and associated wave forces, Society of Petroleum Engineers Journal 21(01) (1981) 129-140.
[16] C. J. Fitzgerald, P. H. Taylor, R. E. Taylor, J. Grice, J. Zang, Phase manipulation and the harmonic components of ringing forces on a surface-piercing column, Proc. R. Soc. Lond. A 470 (2014) 20130847.

[17] J. Zang, P. H. Taylor, G. Morgan, M. Tello, J. Grice, J. Orszaghova, Experimental study of non-linear wave impact on offshore wind turbine foundations, In Coastlab - 3rd International Conference on the Application of Physical Modelling to Port and Coastal Protection. University of Bath. (2010).
[18] M. Coantic, A. Ramamonjiarisoa, P. Mestayer, F. Resch, A. Favre, Wind water tunnel simulation of small scale ocean atmosphere interactions, J. Geophys. Res. C7 (1981) 6607–6626.
[19] H. Jeffreys, On the formation of water waves by wind, Proc. R. Soc. Lond. A, 107 (742) (1925) 189-206.
[20] M.D. Powell, P.J. Vickery, T.A. Reinhold, Reduced drag coefficient for high wind speeds in tropical cyclones, Nature 422, (2003) 279-283.
[21] M.D. Powell, High Wind Drag Coefficient and Sea Surface Roughness in Shallow Water. Final Report to the Joint Hurricane Testbed, (2008), NOAA HRD-AOML report. https://www.nhc.noaa.gov/jht/07-09reports/final_Powell_JHT08.pdf
[22] B. Le Méhauté, An Introduction to Hydrodynamics and Water Waves Volume II, Water Wave Theories. *Springer* (1976).
[23] S. S. Kjeldsen, D. Myrhaug, Breaking waves in deep water and resulting wave forces, In the 11th Offshore Technology Conference (1979).
[24] C. P. Mahalanobis, On the generalised distance in statistics, Proceedings of national institute of Science of India (1936). 49-55.
[25] W.G. Van Dorn, Boundary dissipation of oscillatory waves, Journal of Fluid Mechanics 24 (1966) 769-779.
[26] W. Miles, Surface-wave damping in closed basins, Proc. Roy. Soc. A 297 (1967) 459-473
[27] A. Ghadirian, M. H Vedsted, S. Carstensen, E. C. Damgaard, H. Bredmose, Wave-current interaction effects on waves and their loads on a vertical cylinder, Coastal Engineering – in press.
[28] M. Huseby, J. Grue, Experimental investigation of higher harmonic forces on a vertical cylinder in long waves, 13th international workshop on water waves and floating bodies, Aplhen aan der Rijn, Netherland 414 (2000) 43-46
[29] D. Sarkar, P.H. Taylor, T.A.A. Adcock, H. Bredmose, Harmonic content of wave loads on a column in random unidirectional and directional spread seas - submitted to Journal of Ocean Engineering and Marine Energy (2021).

Webpages:
[30] Storm og ekstrem vind i Danmark – Opgørelser og analyser til og med 2015. Danish Meteorological Institute.
https://www.dmi.dk/fileadmin/Rapporter/TR/tr11-12.pdf, J. Cappelen, 2016 (assessed December 2020) 10